



## Article

# Nanogranular Strontium Ferromolybdate/Strontium Molybdate Ceramics—A Magnetic Material Possessing a Natural Core-Shell Structure

Gunnar Suchaneck <sup>1,\*</sup> , Evgenii Artiukh <sup>2</sup> , Nikolay Kalanda <sup>2</sup>, Marta Yarmolich <sup>2</sup> and Gerald Gerlach <sup>1</sup> <sup>1</sup> Solid-State Electronics Laboratory, TU Dresden, 01062 Dresden, Germany; gerald.gerlach@tu-dresden.de<sup>2</sup> Cryogenic Research Division, SSPA “Scientific-Practical Materials Research Centre of NAS of Belarus”, 220072 Minsk, Belarus; sirfranzferdinand@yandex.ru (E.A.); kalanda362@gmail.com (N.K.); martochka\_ymv@mail.ru (M.Y.)

\* Correspondence: gunnar.suchaneck@tu-dresden.de

**Abstract:** In this work, we demonstrate the preparation of easy-to-fabricate nanogranular strontium ferromolybdate/strontium molybdate core-shell ceramics and examine their properties, including tunnel magnetoresistance, magnetic field sensitivity, and temperature coefficient of the tunnel magnetoresistance. The tunnel magnetoresistance of nanogranular strontium ferromolybdate/strontium molybdate core-shell ceramics was modeled, yielding values suitable for magnetoresistive sensor applications. Such structures possess a narrow peak of magnetic flux sensibility located at about 80 mT. For magnetic flux measurement, single-domain granules with superparamagnetic behavior should be applied. The predicted TMR magnetic flux sensitivities for granules with superparamagnetic behavior amount to about 7.7% T<sup>-1</sup> and 1.5% T<sup>-1</sup> for granule sizes of 3 nm and 5 nm, respectively. A drawback of the tunnel magnetoresistance of such nanogranular core-shell ceramics is the unacceptably large value of the temperature coefficient. Acceptable values, lower than 2% K<sup>-1</sup>, are obtained only at low temperatures (less than 100 K) or large magnetic flux densities (exceeding 6 T). Therefore, a Wheatstone bridge configuration should be adopted for magnetoresistive sensor design to compensate for the effect of temperature.

**Keywords:** strontium ferromolybdate; nanogranular structure; core-shell ceramics; tunnel magnetoresistance; magnetic flux sensitivity; temperature coefficient



**Citation:** Suchaneck, G.; Artiukh, E.; Kalanda, N.; Yarmolich, M.; Gerlach, G. Nanogranular Strontium Ferromolybdate/Strontium Molybdate Ceramics—A Magnetic Material Possessing a Natural Core-Shell Structure. *Electron. Mater.* **2024**, *5*, 1–16. <https://doi.org/10.3390/electronicmat5010001>

Academic Editor: Wojciech Pisula

Received: 15 November 2023

Revised: 25 January 2024

Accepted: 27 January 2024

Published: 31 January 2024



**Copyright:** © 2024 by the authors. Licensee MDPI, Basel, Switzerland. This article is an open access article distributed under the terms and conditions of the Creative Commons Attribution (CC BY) license (<https://creativecommons.org/licenses/by/4.0/>).

## 1. Introduction

In 1994, a large tunnel magnetoresistance (TMR) of 8% at 1.2 T and room temperature was obtained in Co-Al-O nanogranular films with a resistivity of about 100 mΩ × cm [1]. These films consist of two phases: superparamagnetic metallic Co granular grains and Al<sub>2</sub>O<sub>3</sub> narrow intergrains. In such structures, the electrical conductance is governed by tunneling between Co grains through Al<sub>2</sub>O<sub>3</sub> intergrains. Later in 2001, TMR values up to about 14% at room temperature and 1 T were obtained in nanogranular 32 vol%(Fe<sub>0.51</sub>Co<sub>0.49</sub>)–(Mg–F) thin films [2]. Here, the (Mg–F) intergrains were in the crystalline MgF<sub>2</sub> state, enabling a higher TMR compared to Co-Al-O film with an amorphous structure of the Al-oxide intergrain. Thin magnetic films of La<sub>2/3</sub>Ba<sub>1/3</sub>MnO<sub>x</sub> grown epitaxially on SrTiO<sub>3</sub> substrates by off-axis laser deposition at room temperature exhibit an intrinsic magnetoresistance of 60% under a field of several Teslas [3]. Later, this effect was denoted as colossal magnetoresistance (CMR). In polycrystalline La<sub>2/3</sub>Sr<sub>1/3</sub> ceramics, an unusually large low-field (<5 T) magnetoresistance (MR) was obtained, possessing a magnetic field sensitivity of 2–3% T<sup>-1</sup> [4]. This MR is dominated by spin-polarized tunneling enhanced by a high degree of spin polarization.

Similar mechanisms occur in Sr<sub>2</sub>FeMoO<sub>6-δ</sub> (SFMO) ceramics, where the transport properties are dominated by spin-polarized intergrain tunneling through insulating grain

boundaries [5]. Under specific synthesis conditions, SFMO ceramics consist of SrMoO<sub>4</sub> (SMO) intergrain energy barriers between conductive bulks of SFMO grains induced by a small oxygen excess during material fabrication [6]. The ease of forming SMO shells around SFMO grains simply by excess oxygen during synthesis makes SFMO an easy-to-fabricate, natural core-shell material.

A consequence of intergrain tunneling in such SFMO/SMO core-shell structures is the large low-field magnetoresistance obtained in SFMO ceramics [7–9], which is equivalent to the corresponding MR of manganites [4]. Here, the magnetoresistance is governed by the sample microstructure (especially the grain size and the thickness of the dielectric intergrain layers) [10]. Samples with smaller grain sizes are preferable as they demonstrate greater magnetoresistance [11].

In a recent study, the intergranular resistivity, tunnel magnetoresistance, and magnetic field sensibility of superparamagnetic (SPM) and ferro(ferri)magnetic (FM) granular materials were examined theoretically [12]. Starting with the tunnel resistance of a granular metal network in which the grains are interconnected by insulating barriers, the tunnel magnetoresistance was calculated considering the temperature dependencies of magnetization, spin polarization, and both the temperature and magnetic flux dependencies of magnetization as well as the tunneling barrier height. However, nanogranular SFMO/SMO core-shell ceramics have not been adequately addressed in [12]. This gap is now closed in this work, where we validate the tunnel magnetoresistance model by means of our own previously published data of material synthesized by the same procedure, and we consider for the first time the magnetic field sensitivity and the temperature coefficient of tunnel magnetoresistance in SFMO/SMO core-shell structures. The knowledge of these parameters is of great interest with respect to the requirements of corresponding device applications.

## 2. Materials and Methods

### 2.1. Materials Synthesis Methods

The citrate-gel technique was used for the synthesis of nanogranular SFMO ceramics using ultra-high-purity Sr(NO<sub>3</sub>)<sub>2</sub>, Fe(NO<sub>3</sub>)<sub>3</sub>•9H<sub>2</sub>O, (NH<sub>4</sub>)<sub>6</sub>Mo<sub>7</sub>O<sub>24</sub>, and citric acid monohydrate C<sub>6</sub>H<sub>8</sub>O<sub>7</sub>•H<sub>2</sub>O as initial reagents. To obtain a colloidal sol, aqueous solutions of Sr(NO<sub>3</sub>)<sub>2</sub> and Fe(NO<sub>3</sub>)<sub>3</sub>•9H<sub>2</sub>O were mixed in a molar ratio of Sr/Fe = 2:1. Citric acid was added to the solution in a molar ratio of citric acid/Fe = 6.5:1. After that, an aqueous solution of (NH<sub>4</sub>)<sub>6</sub>Mo<sub>7</sub>O<sub>24</sub> was added to the solution of strontium and iron nitrates in a molar ratio of Mo/Fe = 1:1. Then, ethylenediamine was added with constant stirring by means of an IKA C-MAG HS7 magnetic stirrer until the pH of the solution reached 4. Thereafter, the substance was dried at a temperature of 80 °C. The resulting precipitate was placed in a furnace at a temperature of 100 °C, followed by heating at a rate of 0.4 °C min<sup>-1</sup> up to 200 °C, a dwell time of 18 h, and a cooling-down with the time constant of the furnace. The resulting solid foam was crushed and then subjected to heat treatment at 500 °C in an oxygen atmosphere under the pressure  $p(\text{O}_2) = 0.21 \times 10^5$  Pa for 10 h. The final SFMO synthesis was carried out in a reducing ambient atmosphere of a 5% H<sub>2</sub>/Ar gas mixture at 900 °C for 4 h in several stages. Single-phase SFMO powders were pressed into tablets with a diameter of 10 mm and a thickness of 3 mm under a pressure of 4 GPa at 530 °C for 1 min. Dielectric SMO shells were formed in these samples on the surface of the SFMO grains by annealing at 530 °C in an Ar flow with a rate of 11 sccm for 5 h. Since the SFMO powders were agglomerated, ultrasonic dispersion [13,14] was used to obtain highly dispersed particles with an average size smaller than 100 nm. Ethyl alcohol was chosen as a liquid medium since there is neither chemical interaction with SFMO nor SFMO decomposition. Details of sample fabrication were already described elsewhere [9,15,16].

### 2.2. Materials Characterization

The ultrasound dispersion has been implemented by the Bandelin HD2200 setup. Measurements of the SFMO individual grain size were carried out by means of the dynamic

light scattering (DLS) technique using the Zetasizer nanoparticle analyzer. Additionally, the grain size was evaluated using a NT-206 atomic force microscope.

The phase composition and the degree of superstructural ordering were determined using the ICSD–PDF2 (Release 2000) database. The XRD patterns were recorded by X-ray diffraction measurements using an Empyrean diffractometer (Malvern PANalytical, Malvern, UK) in Cu-K $\alpha$  radiation at room temperature in the angle range  $2\theta = 10\text{--}90^\circ$  with step  $\Delta 2\theta = 0.026^\circ$ .

Electrical resistivity and MR were investigated by means of a commercial vibrating sample magnetometer (Cryogenic Ltd., London, UK) in the temperature range from 4 to 300 K in constant magnetic fields up to 8 T. The measurements were carried out upon commutation of the magnetic field and electrical current in order to avoid the impact of parasitic thermopower.

SEM measurements were performed using a JEOL JSM-7000F field emission scanning electron microscope.

### 2.3. Modeling Equations

In the dielectric regime, electrical conduction of granular materials results from the transport of electrons and holes by tunneling from one isolated metallic grain to the next. A charge carrier in a granular material contributes to electrical conductivity when an electron is removed from a neutral grain and placed on a neighboring neutral grain. Such a process requires charging energy  $E_c$  per grain, as shown [17]:

$$E_c = \frac{e^2}{d} F(w, d), \quad (1)$$

where  $e$  is the electronic charge,  $d$  is the granular or grain size,  $w$  is the separation between the grains (e.g., the tunneling barrier width), and  $F(w, d)$  is a function whose form depends on the shape and arrangement of the grains. Assuming the grain size  $d$  to be much larger than the barrier width  $w$ ,  $E_c$  is approximately given by [18]:

$$E_c \approx \frac{4e^2 w}{\varepsilon \varepsilon_0 d^2}, \quad (2)$$

with  $\varepsilon$  and  $\varepsilon_0$  are the dielectric and vacuum permittivities, respectively. Since the charging energy is reciprocal to the grain diameter, charging effects become significant at small grain sizes.

A  $\ln\sigma$  versus  $T^{-1/2}$  plot with  $\sigma$  as the electrical conductivity yields a parameter  $C$  describing the apparent thermal activation energy of the conductivity in the case of tunneling between two neighboring grains, as shown [18,19]:

$$C = w\chi E_c, \quad (3)$$

where, in our case,  $w\chi$  is a value in the order of about 2 [20,21].

In the next step, we consider a metal network in which the metal grains are interconnected by insulating barriers. The positive–negative pairs of charged grains induced by electron tunneling through the barriers are assumed to be roughly of the same size. In this case, each grain contributes about half of the charging energy  $E_c$ , resulting in a density of charge carriers proportional to  $\exp(-E_c/2kT)$ . Thus, the resistivity caused by tunneling is given by [18,19]:

$$\rho_T = \rho_0 \exp\left(f\chi w + \frac{E_c}{2kT}\right), \quad (4)$$

where  $f$  is a barrier shape factor with  $f = 2$  for rectangular barriers and  $f = \pi/2$  for parabolic barriers, and  $\chi$  is the reciprocal localization length of the wave function:

$$\chi = \sqrt{\frac{2m^*V_0}{\hbar^2}}, \quad (5)$$

with  $m^*$  as the effective electron mass,  $V_0$  as the barrier height,  $\hbar$  as the reduced Planck constant,  $w$  as the barrier width,  $k$  as the Boltzmann constant,  $T$  as the absolute temperature, and  $\rho_0$  as the bulk resistivity. Note that we are considering sufficiently thin barriers in the order of 1–3 nm where direct tunneling occurs, which is not disturbed by localized states in the thin barrier film [22].

Considering the parameter  $C$  in Equation (3) and assuming a rectangular barrier ( $f = 2$ ), the argument of the exponent in Equation (4) becomes:

$$f(w) = 2\chi w + \frac{C}{2\chi w k T}, \quad (6)$$

which possesses a minimum at [18]:

$$w_{\min} = \frac{1}{2\chi} \sqrt{\frac{C}{kT}}. \quad (7)$$

The corresponding resistivity minimum yields [18]:

$$\rho_{\min}(T) \propto \exp \left[ 2\sqrt{\frac{C}{kT}} \right]. \quad (8)$$

The value  $\rho_{\min}(T)$  governs the temperature dependence of the network resistivity  $\rho(T)$  since tunneling occurs by paths, which makes the exponential factor of resistivity the lowest.

The spin-dependent tunneling through a barrier between two ferromagnetic grains is a function of the angle  $\theta$  between the grain magnetizations. Neglecting the correlations between magnetic moments of neighboring grains, the average  $\langle \cos \theta \rangle$  over all pairs of grains for angles between 0 and  $\pi$  represents the square of the relative magnetization  $m^2 = (M/M_s)^2$ , i.e., the ratio of magnetization  $M$  to the saturation one  $M_s$ . Finally, we arrive at an intergrain resistivity amounting to [23]:

$$\rho = \frac{\rho_0}{1 + m^2 P^2} \exp \left[ 2\sqrt{\frac{C}{kT}} \right], \quad (9)$$

with  $P$  as the spin polarization. The intergrain tunnel magnetoresistance of a network of tunnel junctions whose electrodes are double-perovskite grains with an insulating oxide layer in between is given by [24]:

$$TMR = \frac{\rho(B)}{\rho(0)} - 1 \approx \frac{1}{1 + m(B, T)^2 P^2} - 1 = -\frac{m(B, T)^2 P^2}{1 + m(B, T)^2 P^2}, \quad (10)$$

where  $\rho(B)$  is the resistivity for a given magnetic flux density  $B$  and  $m(B, T)$  is the relative magnetization for given values of magnetic flux  $B$  and temperature  $T$ .

In granular systems with a broad distribution in granule size, it is highly probable that large granules are well separated from each other. This is given by the fact that granules are more separated the larger the granule size. As a result, a number of smaller granules exist, separating the large ones. Here, the ordinary tunneling of an electron from a large granule to a small one increases the charging energy  $E_c$  in Equation (2) and suppresses tunneling by the Coulomb blockade at low temperatures. In this case, higher-order tunneling comes into play, i.e., the dominant contribution to the tunneling current now comes from higher-order processes of spin-dependent tunneling where the carrier is transferred from a charged large granule to the neighboring neutral large granule through an array of small granules, using co-tunnelling of  $(n + 1)$  electrons. The TMR is then given by [20]:

$$TMR = \frac{1}{(1 + m^2 P^2)^{1+n^*}} - 1, \quad (11)$$

where

$$n^* = \sqrt{\frac{\langle E_c \rangle}{8\chi^* \langle w \rangle kT}} = \sqrt{\frac{D}{T}}, \quad (12)$$

with  $\chi^* = p\chi$ ,  $p$  is a constant defined in [17], and  $n^*$  is a fitting parameter of the higher-order tunneling processes. Note that we have rewritten Equation (11) according to the definition of magnetoresistance in this work given in Equation (10). In a granular Co-Al-O system,  $n^*(T \rightarrow 0)$  takes a value of 1.6, so that one or two small granules intervene between larger ones in the higher-order processes. Higher-order tunneling increases the TMR at low temperatures. On the other hand, higher-order tunneling is negligible at room temperature since here  $n^*$  tends to equal zero [12].

For  $m^2 P^2 \ll 1$ , Equation (11) simplifies to:

$$TMR \approx - \left( 1 + \sqrt{\frac{D}{T}} \right) \cdot m^2 P^2. \quad (13)$$

In sufficiently small granules, i.e., below a critical size of [12]:

$$d_{cr}^{spm} = \left( \frac{\pi \cdot \ln(\tau_m / \tau_0) \cdot kT}{6 \cdot K(T)} \right)^{1/3}, \quad (14)$$

the magnetization can randomly flip directions under the influence of temperature. This applies to FM metal (Fe, Co) granules and SFMO granules with sizes below 1 nm and 1.7 nm at 4 K as well as sizes below 5–6 nm and 12 nm at 300 K, respectively [12]. In the absence of an external magnetic field, when the time used to measure the magnetization of the nanosized granules is much longer than the typical time between two flips (called Néel relaxation time), the granule magnetization appears to be on average zero. The magnetic behavior resembles that of a paramagnetic, exhibiting an unusually high magnetic susceptibility attributed to a large number of formula units oriented in the same direction within a single magnetic domain. Such a magnetic behavior is known as superparamagnetism. Granular networks of noninteracting superparamagnetic (SPM) granules were already modeled in [12]. The reduced magnetization of SPM granules is determined by the Langevin function  $L$  [25]:

$$m = L(\zeta B) = \coth(\zeta B) - 1/(\zeta B), \quad (15)$$

where  $\zeta = \mu/kT$ , with  $\mu$  as the total magnetic moment of the granule depending on its size.

Tunneling spin polarization and the interface magnetization follow the same temperature dependence [26,27]. As a result, based on the theory of spin waves [28], the spin polarization resembles the spontaneous magnetization behavior at low temperatures, known as Bloch's  $T^{3/2}$  law of variation in saturation moment with temperature near absolute zero:

$$P(T) = P_0(1 - g \cdot T^{3/2}). \quad (16)$$

Here,  $P_0$  is the spin polarization of ordered SFMO at zero temperature, and  $g$  is a fitting parameter, which in the case of magnetization is generally larger for the surface than for the bulk [26]. It is very sensitive to surface contaminants [29]. For the sake of simplicity, Bloch's  $T^{3/2}$  coefficient  $g$  was estimated by means of the Curie temperature  $T_C$ :

$$g = T_C^{-3/2}. \quad (17)$$

They are in satisfactory agreement with previous experimental data of  $0.1\text{--}0.6 \times 10^{-5}$  for Co/Al<sub>2</sub>O<sub>3</sub> [30],  $1.9 \times 10^{-4}$  for La<sub>2/3</sub>Sr<sub>1/3</sub>MnO<sub>3</sub>/SrTiO<sub>3</sub>,  $5.1 \times 10^{-5}$  for La<sub>2/3</sub>Sr<sub>1/3</sub>MnO<sub>3</sub>/

LaAlO<sub>3</sub>,  $1.58 \times 10^{-4}$  for La<sub>2/3</sub>Sr<sub>1/3</sub>MnO<sub>3</sub>/TiO<sub>2</sub> [31], and  $1.31 \times 10^{-4}$  derived from the intergranular TMR in Ba<sub>0.8</sub>Sr<sub>0.2</sub>FeMoO<sub>6</sub> [24].

Now, we take into account that the spin polarization has a similar dependence on the antisite disorder (ASD), that is, the fraction of B-site ions, Fe or Mo, on the wrong sublattice sites, which varies from 0 (corresponding to a complete order) up to 0.5 (describing a completely random Fe-Mo site occupancy) as the magnetization [32]. As a result, the spin polarization  $P$  was calculated following [33] by:

$$P(T) = P_0 \cdot (1 - 2ASD) \cdot (1 - g \cdot T^{3/2}). \quad (18)$$

With regard to Equation (10), the magnetic field sensitivity of granular FM materials amounts to:

$$\frac{dTMR}{dB} = -\frac{2m(B, T)P^2 \cdot \partial m / \partial B}{(1 + m(B, T)^2 P^2)^2}, \quad (19)$$

with

$$\frac{\partial m}{\partial B} = m(T, 0) \cdot \left[ \frac{1}{2} a_{1/2} B^{-3/2} + a_1 B^{-2} + 2a_2 B^{-3} + \dots \right]. \quad (20)$$

For SPM granules, the magnetic field sensitivity yields [12]:

$$\frac{d(TMR)}{dB} = -\frac{2P^2 dL(\zeta B) / dB}{[1 + P^2 L(\zeta B)^2]} = -\frac{2P^2 \zeta \cdot [(\zeta B)^{-2} - \sinh^{-2}(\zeta B)]}{\left\{ 1 + P^2 \cdot [\coth(\zeta B) - 1/\zeta B]^2 \right\}^2}. \quad (21)$$

Temperature affects the measuring accuracy of any sensor. Thus, there always remains a small temperature inaccuracy in the considered temperature range, despite a number of compensation measures. This inaccuracy is often expressed as the temperature coefficient (TC). It expresses the relationship between a change in the sensing physical property and the change in temperature that causes it. Consequently, it represents the relative change in the sensing physical property with a given change in temperature. Correspondingly, the TC of the TMR is given by:

$$TC_{TMR} = \frac{1}{TMR} \cdot \frac{d(TMR)}{dT}. \quad (22)$$

The particular case of Equation (13) yields a temperature coefficient of the TMR amounting to:

$$TC_{TMR} = \frac{1}{TMR} \frac{d(TMR)}{dT} = \frac{\sqrt{D}}{2T^{3/2}(1 + \sqrt{D/T})}. \quad (23)$$

In the calculations of this work, numerical derivatives of experimental data were evaluated by approximating experimental curves by quartic polynomials.

### 3. Results and Discussion

In samples synthesized as described in Section 2.1, X-ray diffraction analysis revealed the presence of reflections of the SFMO (ICSD-99933) and the SMO (ICSD-28025) phases (Figure 1). At room temperature, SFMO has a structure with tetragonal symmetry and space group  $I4/m$ , and the lattice constants and cell volume are respectively equal to  $a = b = 5.57(1) \text{ \AA}$ ,  $c = 7.89(2) \text{ \AA}$ , and  $V = 244.93(6) \text{ \AA}^3$ . SMO has a structure with tetragonal symmetry with space group  $I4_1/a$ , with lattice and cell volume constants equal to  $a = b = 5.39(4) \text{ \AA}$ ,  $c = 12.01(7) \text{ \AA}$ , and  $V = 349.63(7) \text{ \AA}^3$ .

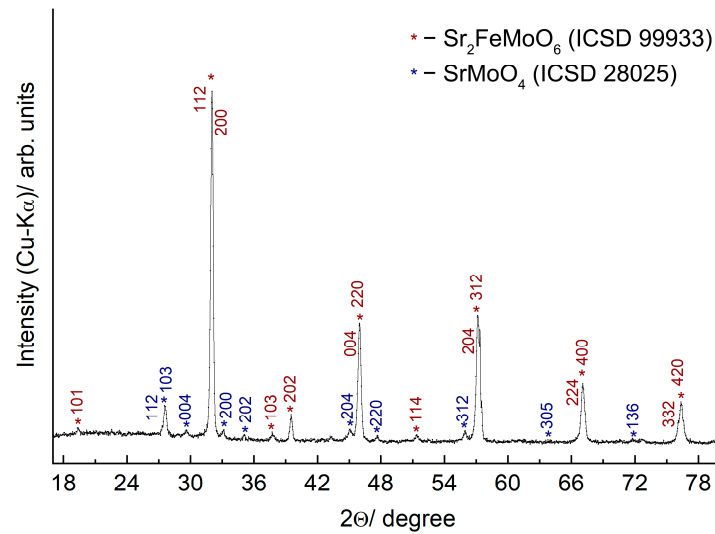


**Figure 1.** X-ray diffraction pattern of an SFMO/SMO sample.

The growth of continuous dielectric shells in the form of the  $\text{SrMoO}_4$  phase on SFMO grains has been established by means of microstructural analysis data (Figure 2). The EDX pattern of point 1 (core) corresponds to that of an SFMO reference sample, while the EDX pattern of point 2 (shell) corresponds nearly to that of SMO. Some Fe is also visible at point 2, since the size of the region excited by the electron beam exceeds the small thickness of the shell.

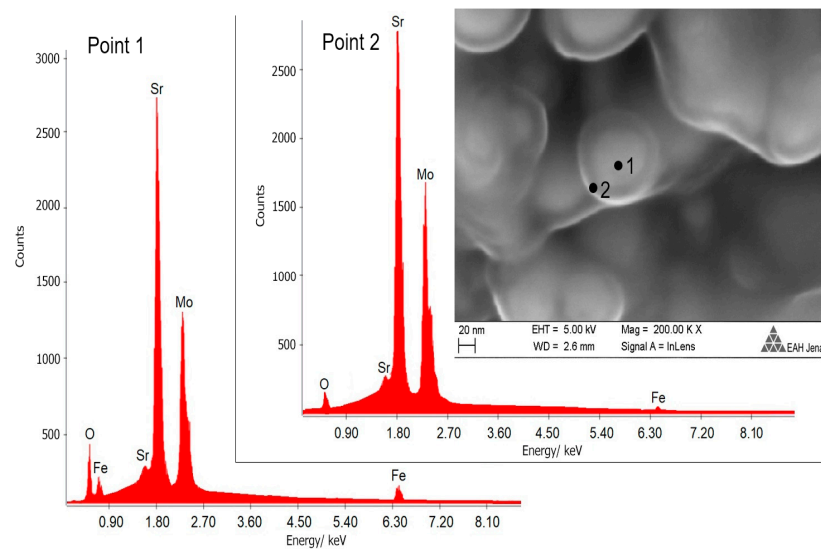


**Figure 2.** Image of the microstructure of an SFMO/SMO sample and its elemental composition at points 1 and 2.

The nanoparticle size distribution was analyzed by means of DLS (Figure 3). It is most widely represented by the following lognormal distribution:

$$f(d) = \frac{1}{\sqrt{2\pi}\sigma} \exp\left[-\frac{\ln(d) - \ln(\langle d \rangle)}{2\sigma}\right], \quad (24)$$

where  $d$ ,  $\langle d \rangle$ , and  $\sigma$  are the diameter, average diameter, and dispersion of the particle size distribution, respectively. The calculated average particle diameter according to Equation (24) for a nano-sized powder subjected to ultrasonic dispersion for 60 min is  $\langle d \rangle = 70.8$  nm. In this case, the dispersion of the particle size distribution of SFMO corre-

sponds to  $\sigma = 0.243$  nm. The coefficient of determination  $R^2$  of the measured distribution with a log-normal distribution function amounts to 0.997, which confirms the good match.

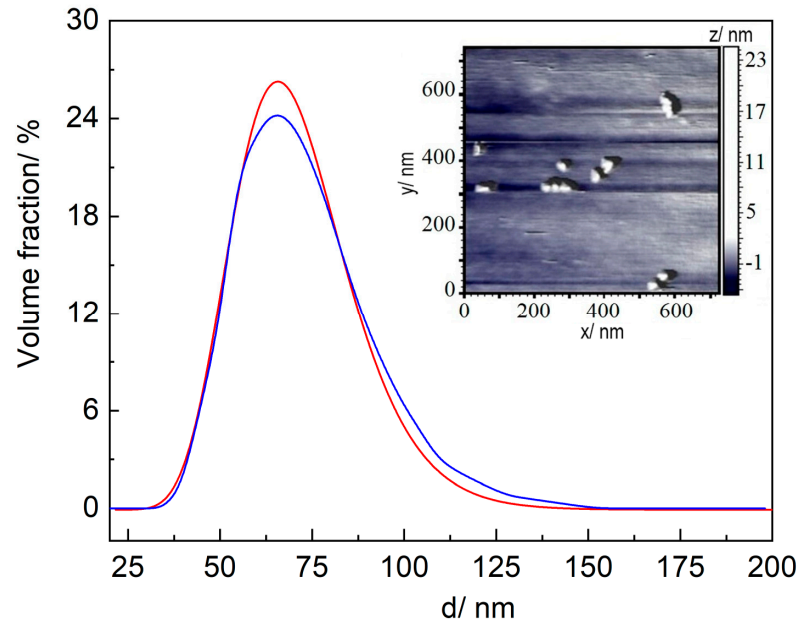


**Figure 3.** Size distribution of the volume fraction of the SFMO particle ensemble after ultrasonic dispersion according to DLS analysis data (blue line) and its approximation by a log-normal distribution function  $f(d)$  (red line). Inlet: AFM image of SFMO powder grains.

In the case of nanogranular SFMO/SMO core-shell ceramics fabricated by the citrate-gel method with  $d \approx 70$  nm and  $w = 1.24$  nm [9], and assuming  $\varepsilon_{\text{SrMoO}_3} \approx 10$  [34], the charging energy  $E_c$  in Equation (1) amounts to a value of  $E_c \approx 1.6$  meV. This should be compared with a value of  $E_c \approx 1$  meV obtained after saturation of the insulating SMO phase at grain boundaries in mechanically ball-milled polycrystalline SFMO pellets [35]. Such ball-milled powders possess a grain size of about 100 nm after 6 h of grinding [36], i.e., approximately the same grain size as the considered nanogranular SFMO/SMO core-shell ceramics.

Using the  $\ln\sigma$  versus  $T^{-1/2}$  plot, we find a parameter  $C$  related to  $E_c$  (cf. Equation (3)), with  $C \approx 4.7$  meV for zero magnetic field conductivities of our nanogranular SFMO/SMO core-shell ceramics fabricated by the citrate-gel method in the temperature range of 10–50 K. The  $C$  values of Co-Al-O insulating granular films were 9.48 meV for  $\text{Co}_{36}\text{Al}_{22}\text{O}_{42}$ , 2.15 meV for  $\text{Co}_{46}\text{Al}_{19}\text{O}_{35}$ , 1.55 meV for  $\text{Co}_{52}\text{Al}_{20}\text{O}_{28}$ , and 0.78 meV for  $\text{Co}_{54}\text{Al}_{21}\text{O}_{25}$  [20]. In other insulating granular metal films, the  $\ln\sigma$  versus  $T^{-1/2}$  plot results in much higher  $C$  values, decreasing with increasing metal fraction from 1.1 eV (0.08%) to 0.13 eV (0.44%) in Ni-SiO<sub>2</sub> composites, from 1.1 eV (0.04%) to 0.20 eV (0.18%) in Pt-SiO<sub>2</sub> composites, and from 120 meV (0.18%) to 4 meV (0.38%) in Au-Al<sub>3</sub>O<sub>4</sub> composites [18].

Both the temperature dependence and the field dependence of the relative magnetization  $m$  of FM SFMO were calculated following reference [37]. For the temperature dependence, this yields:

$$m^2(T, B = 0) = \sum_i a_i \left( \frac{T_C - T}{T_C} \right)^i. \quad (25)$$

Using  $m(T)$  values from [24,38], we obtained  $a_1 = 1.89$ ,  $a_2 = -1.97$ ,  $a_3 = 2.2$ , and  $a_4 = -1.14$  for the coefficients of Equation (25) [37].

At sufficiently high magnetic fluxes, when magnetic interactions may still be neglected, the magnetic flux density dependence of  $m$  may be modeled by means of a traditional

analysis of the approach of magnetization to saturation [39,40]. As a result, the magnetic flux dependence of the relative magnetization is given by:

$$m(B) = 1 - \sum_i \left( \frac{b_{i/2}}{B} \right)^{i/2} + \kappa B, \quad (26)$$

with  $i = 1, 2, 3, 4$  for point, line, and plane forces as well as uniform volume forces, respectively.

The  $\kappa B$  term is often referred to as the so-called paramagnetism-like term [41]. It represents the high-field magnetization resulting from an increase in spontaneous magnetization by the application of a field [42]. At temperatures well below the Curie point, this term is usually small and may often be neglected [43] (p. 325).

Point defects in ceramics and granular materials are concentrated at grain boundaries, representing only a small part of the total sample volume. Consequently, the  $(b_{1/2}/B)^{1/2}$  term will be small or even negligible at higher magnetic fluxes. The value of  $b_{1/2} = 0.00085 \text{ T}^{1/2}$ , derived based on data in [44,45], will play a role only at small magnetic fluxes of  $B < 85 \text{ mT}$ .

The  $b_1/B$  term in Equation (26) is referred to as the magnetic hardness [41]. It has been observed to be constant at high magnetic fluxes [46] and was attributed to internal stresses produced by dislocations [39], especially by pairs of dislocations of opposite sign separated by a short distance smaller than the magnetic decay distance [47]. Another theory attributes  $b_1$  to the leakage field in ferromagnetic materials [48]. In general, this constant is attributed to inclusions or microstress [43] (p. 325). For example, it represents the demagnetizing effects of inhomogeneities such as grain boundaries, dislocations, and nonmagnetic inclusions [46].

The  $b_2/B^2$  term in Equation (26) is attributed to crystal anisotropy [41]. Furthermore, it was shown that dislocation pairs of different signs separated by a long distance and surplus dislocations of one sign contribute to this term [47]. The  $b_2/B^2$  term is dominant for extremely high magnetic fluxes, while the  $b_1/B$  term is dominant at intermediate magnetic fluxes [49]. Thus, the  $b_1/B$  term is effective only in a limited field range. If one only considers the term  $b_1/B$  for nanogranular SFMO/SMO core-shell ceramics made by means of the citrate gel method [50], the  $m(B)$  characteristic is well approximated by  $b_1 = 0.05 \text{ T}$  below  $0.1 \text{ T}$ ,  $b_1 = 0.085 \text{ T}$  in the region  $0.3\text{--}1 \text{ T}$ , and  $b_1 = 0.02 \text{ T}$  in the region  $1.5\text{--}4 \text{ T}$ . On the other hand, the  $m(B)$  curve of a similar sample measured in a different setup [51] in this approach yields  $b_1 \approx 0.3 \text{ T}$  for magnetic fluxes in the range  $2\text{--}10 \text{ T}$ . The values given by the authors of [51] are  $b_1 = 0.968 \text{ T}$  and  $b_2 = 0.00292 \text{ T}^2$ .

Neglecting the influence of internal strain, a theoretical value of the coefficient of the  $b_2/B^2$  term, which is attributed to magnetocrystalline anisotropy (MA), is given by [52]:

$$b_2^{MA} \approx \frac{8}{105} \cdot \left( \frac{2K_1}{M_s n} \right)^2, \quad (27)$$

with  $K_1$  as the uniaxial anisotropy constant and  $n$  as the volumetric density of the formula units (f.u.), that is, the inverse of the formula unit volume. Here, the numerical coefficient  $8/105$  applies to the cubic anisotropy of randomly oriented polycrystalline samples. Table 1 compiles the values of  $b_2^{MA}$  calculated using Equation (27) for a saturated magnetization of  $M_s = 2.6 \mu_B \text{ f.u.}^{-1}$  and  $n = 8.024 \times 10^{27} \text{ f.u. m}^{-3}$  using different values of the uniaxial anisotropy constant  $K_1$ . Note that a wide range of values for  $K_1$  leads to a large uncertainty in the coefficient  $b_2^{MA}$ .

**Table 1.** Parameter  $b_2^{MA}$  calculated for different values of the uniaxial anisotropy constant  $K_1$ .

$K_1, \text{J m}^{-3}$	Ref.	$b_2^{MA}, \text{T}^2$
$5 \times 10^3$	[50]	$2.035 \times 10^{-4}$
$1.99 \times 10^4$	[51]	$3.224 \times 10^{-3}$
$2.74 \times 10^4$	[53]	$6.112 \times 10^{-3}$
$1.7 \times 10^5$	[54]	$2.353 \times 10^{-1}$

The contribution of internal strain (IS) to  $b_2$  is given by [55]:

$$b_2^{IS} = \frac{3}{5} \cdot \left( \frac{\lambda_s \langle \sigma_i \rangle}{M_s n} \right)^2, \quad (28)$$

where  $\lambda_s$  is the coefficient of magnetostriction and  $\sigma_i$  is the internal strain. Taking  $\lambda_s = 10^{-4}$  [43,56] and  $\langle \sigma_i \rangle = 150 \text{ MPa} - 600 \text{ MPa}$  [57], we arrive at  $b_2^{IS} = 0.0015 - 0.0240 \text{ T}^2$ .

The coefficient  $b_3/B^3$  of Equation (26), which is also determined by magnetocrystalline anisotropy, may be written for the cubic anisotropy of randomly oriented polycrystalline samples as [58,59]:

$$b_3^{MA} \approx \frac{8}{105} \cdot \frac{72}{11 \cdot 13} \cdot \left( \frac{K_1}{M_s n} \right)^3 \approx 0.03836 \cdot \left( \frac{K_1}{M_s n} \right)^3. \quad (29)$$

However, this term is negligible compared to the  $b_2/B^2$  term at magnetic fluxes  $B > K_1/M_s n$  (0.1...0.5 T in our case). Since the coefficients  $b_i$  are sensitive to point defects (vacancies, antisite positions, and impurity ions), line defects (dislocations), and area defects (stacking faults, grain, twin, and antiphase boundaries), they are highly dependent on the synthesis conditions of the SFMO ceramics.

For comparison, we consider Fe and Co applying a phenomenological model of the temperature dependence of the relative magnetization given by [60]:

$$m(T) = \left[ 1 - \left( \frac{T}{T_C} \right)^p \right]^\beta. \quad (30)$$

The corresponding fitting parameters  $p$  and  $\beta$  are compiled in Table 2.

**Table 2.** Fitting parameters of Equation (30) [60].

Compound	$p$	$\beta$
Fe	2.876	0.339
Co	2.369	0.34

Table 3 compiles the parameters used for the calculations in this work.

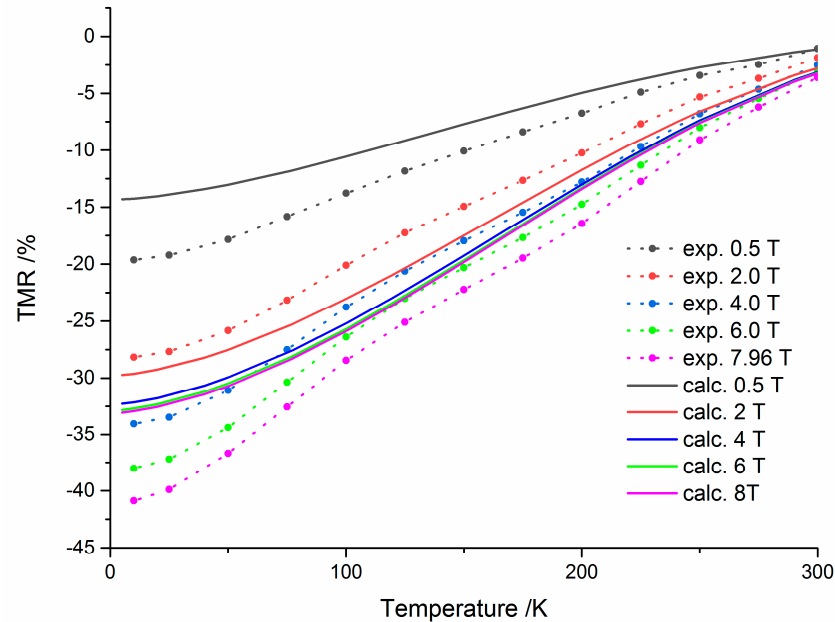
**Table 3.** Parameters used for calculations in this work.

Compound	$P_0$	Ref.	$T_C, \text{K}$	Ref.	$a_i$	Ref.	$b_{i/2}, \text{T}^{i/2}$	Ref.
SFMO	0.72 <sup>(1)</sup>	[37]	420	[38]	$a_1 = 1.89$ $a_2 = -1.97$ $a_3 = 2.2$ $a_4 = -1.14$	[38]	$b_{1/2} = 0$ $b_1 = 0.085$ $b_2 = 0.115$ $b_3 = 0.118$	[37]
Co	0.34	[61]	1388	[62]	Equation (30)	[60]	$b_2 = 0.042$	[59]
Fe	0.44	[61]	1043	[62]	Equation (30)	[60]	$b_2 = 0.050$	[63]

<sup>(1)</sup> ASD = 0.1.

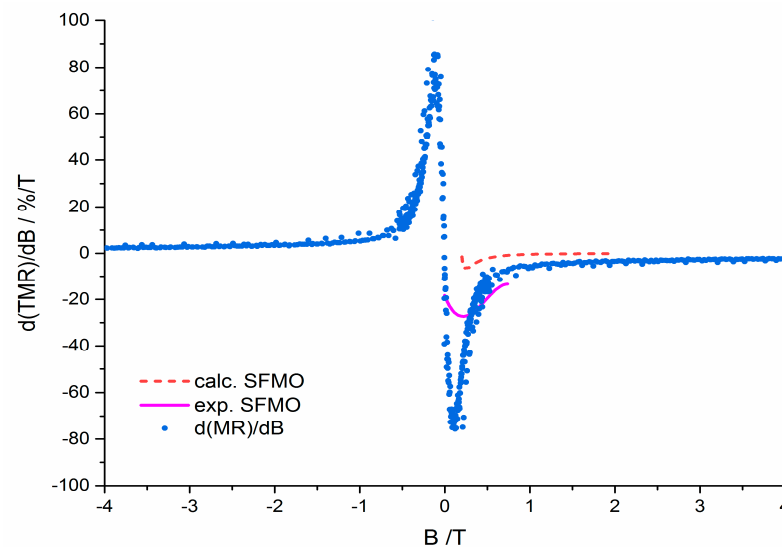
Figure 4 illustrates a comparison of the TMR values, calculated by means of Equation (10), with experimental data of nanogranular SFMO/SMO core-shell ceramics from [15]

fabricated by the same procedure. While the temperature dependence is well reproduced, the magnetic flux dependence is satisfactorily described only in the middle region of  $B$ , where the values of the coefficient  $b_i$  are most valid. Note that the calculated field dependence of the magnetoresistance strongly depends on the coefficients of Equation (26), which are subject to large uncertainties. As a result, the achieved TMR values are suitable for practical applications.



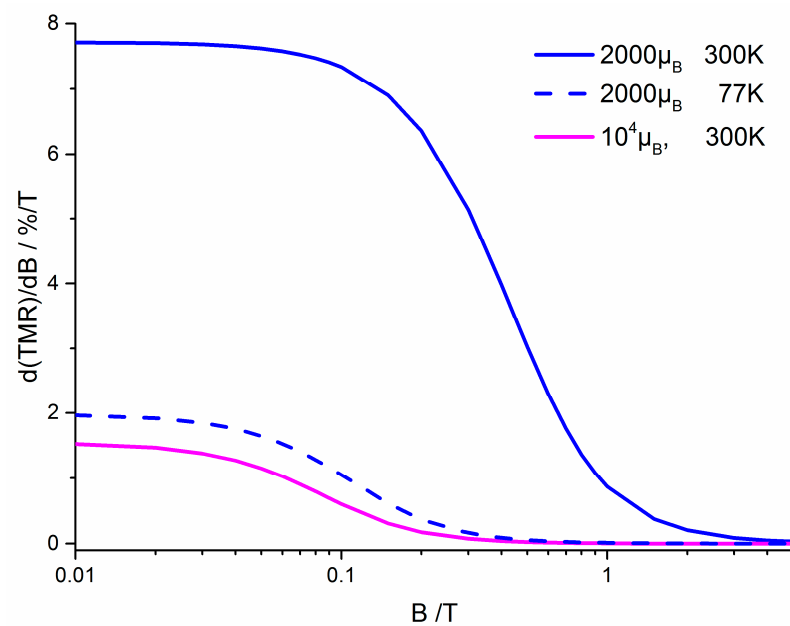
**Figure 4.** Comparison of the TMR values calculated by means of Equation (10) with experimental data of nanogranular SFMO/SMO core-shell ceramics from [15].

Figure 5 represents the experimental magnetic field sensitivity of FM nanogranular SFMO/SMO core-shell ceramics. The shown curve is in good qualitative agreement with experimental data at 10 K of ceramic SFMO, which were annealed in a reducing atmosphere [64] and with calculations from [12] for nanosized SFMO ceramics using Equation (10).



**Figure 5.** Magnetic field sensitivity of nanogranular SFMO/SMO core-shell ceramics fabricated by the citrate gel method in comparison with experimental data of ceramic SFMO [64] and with calculations from [12] for nanosized SFMO ceramics using Equation (19).

The sharp sensitivity peak illustrates that nanosized SFMO/SMO core-shell granules are not suitable as a magnetic field sensor. For this purpose, superparamagnetic granules should be used. This is illustrated in Figure 6, which depicts the magnetic field sensitivity of superparamagnetic, noninteracting SFMO granules calculated by means of Equation (21). Taking our SFMO unit cell volume of  $V = 2.45 \times 10^{-28} \text{ m}^3$ , a saturation magnetization of  $\mu = 2.6 \mu_B \text{ f.u.}^{-1}$  for material synthesized by the same procedure [51,65], and assuming a density of 98% of the theoretical one, a total magnetic moment of a granule amounting to  $\mu = 2000 \mu_B$  corresponds to a granule size of about 3 nm, while a value  $\mu = 10^4 \mu_B$  corresponds to a granule size of about 5 nm. Since the spin polarization of SFMO is significantly higher than that of Co and Fe, the magnetic field sensitivity of SFMO will be correspondingly larger.



**Figure 6.** Magnetic field sensitivity of superparamagnetic noninteracting SFMO granules possessing a total magnetic moment of  $2000 \mu_B$  and  $10^4 \mu_B$ , respectively.

In contrast to ferromagnetic SFMO granules, superparamagnetic ones provide a nearly constant magnetic field sensitivity at low magnetic fields up to 400 mT, which is beneficial for low-field magnetic sensor applications (Figure 6). The predicted TMR magnetic flux sensitivities for granules with superparamagnetic behavior amount to about  $7.7\% \text{ T}^{-1}$  and  $1.5\% \text{ T}^{-1}$  at room temperature for granule sizes of 3 nm and 5 nm, respectively.

Figure 7 shows the temperature coefficients of nanogranular SFMO/SMO core-shell ceramics deduced from the numerical derivatives of the experimental data in Figure 4 in comparison with data of Fe and Co low field values deduced from the numerical derivative of the TMR calculated by means of Equation (10) using Equations (17), (18), and (30), as well as data of superparamagnetic SFMO at 100 mT deduced from the numerical derivative of the TMR calculated by means of Equation (10) using Equations (15), (17), and (18). The relatively small TC of ferromagnetic Co and Fe is a consequence of their much weaker temperature dependence of the spin polarization attributed to higher Curie temperatures. Since the TC value of SPM SFMO reduces with increasing magnetic flux, superparamagnetic SFMO is superior to ferrimagnetic SFMO/SMO core-shell structures, with the exception of at very low temperatures. Note that Equation (23), which is valid for small  $m^2 P^2 \ll 1$ , yields a positive TC decreasing with magnetic flux. In the case of strongly disordered SFMO, the TC is in the order of  $0.1\% \text{ K}^{-1}$ . According to Equation (11), co-tunneling of  $(n + 1)$  electrons by carrier transfer from a charged large granule to the neighboring neutral large granule through an array of small granules increases the TC. Considering an acceptable TC in the order of  $2\% \text{ K}^{-1}$ , nanogranular SFMO/SMO core shell ceramics are suitable

for application only at low temperatures (less than 100 K) or high magnetic flux densities (exceeding 6 T).

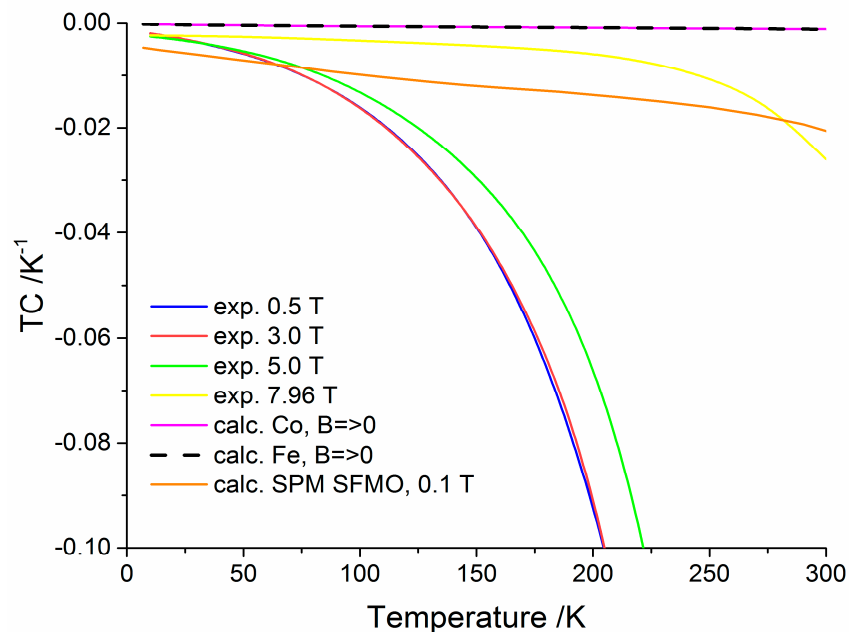


**Figure 7.** Temperature coefficients of the TMR of nanogranular SFMO/SMO core-shell ceramics deduced from the numerical derivatives of the experimental data in Figure 4 in comparison with calculated data of Fe and Co as well as calculated data of superparamagnetic SFMO.

#### 4. Conclusions

This work demonstrates the creation of the  $\text{Sr}_2\text{FeMoO}_{6-\delta}$  (SFMO) nanogranular ceramics, where the granules were covered with  $\text{SrMoO}_4$  (SMO) dielectric shells of about 1 nm thickness (SFMO/SMO core-shell structure). Based on the modeling of the tunnel magnetoresistance, it was shown that the fabricated SFMO/SMO structures are suitable for magnetoresistive sensors. However, it was found that SFMO/SMO core-shell structures have a narrow peak of magnetic flux sensitivity at about 80 mT, which hinders their practical use. This may be avoided by applying paramagnetic granules of smaller size. We predict that single-domain SFMO granules with superparamagnetic behavior provide nearly constant magnetic field sensitivity at low magnetic flux densities up to about 50 mT. Therefore, superparamagnetic granules are well suited for magnetic flux measurements. The predicted TMR magnetic flux sensitivities for granules with superparamagnetic behavior amount to about  $7.7\% \text{ T}^{-1}$  and  $1.5\% \text{ T}^{-1}$  for granule sizes of 3 nm and 5 nm, respectively.

A drawback of the TMR in nanogranular SFMO/SMO core-shell ceramics is the unacceptably large value of the temperature coefficient. Acceptable values of about  $2\% \text{ K}^{-1}$  are obtained only at low temperatures (less than 100 K) or large magnetic flux densities (exceeding 6 T). To compensate for the effect of temperature, a temperature-compensating circuitry should be adopted. One example is a Wheatstone bridge configuration balancing two legs of a bridge circuit, of which one leg includes the unknown component. If the TC of the two legs is identical, the temperature effects are canceled out.

**Author Contributions:** Conceptualization, G.S.; methodology, N.K.; software, E.A.; validation, G.S., N.K. and M.Y.; formal analysis, E.A.; investigation, G.S., N.K. and M.Y.; resources, N.K. and G.G.; writing—original draft preparation, G.S.; writing—review and editing, N.K. and G.G.; visualization, E.A.; supervision, N.K. and G.G.; project administration, N.K. and G.G.; funding acquisition, G.S., N.K. and G.G. All authors have read and agreed to the published version of the manuscript.

**Funding:** This work was funded by the EU project H2020-MSCA-RISE-2017-778308-SPINMULTIFILM and the Belarusian Republican Foundation for Fundamental Research (BRFFR) Project No. F24V-004.

**Data Availability Statement:** The original contributions presented in the study are included in the article; further inquiries can be directed to the corresponding author.

**Acknowledgments:** The authors thank Nikolai A. Sobolev (University of Aveiro) for helpful discussions and suggestions. They are also grateful to Maxim Bushinsky (SSPA, Scientific-Practical Materials Research Centre of the NAS of Belarus) for the measurements of the electro-physical and galvanomagnetic characteristics of the experimental samples.

**Conflicts of Interest:** The authors declare no conflicts of interest.

## References

- Fujimori, H.; Mitani, S.; Ohnuma, S. Tunnel-type GMR in metal-nonmetal granular alloy thin films. *Mater. Sci. Eng. B* **1995**, *31*, 219–223. [[CrossRef](#)]
- Kobayashi, N.; Ohnuma, S.; Masumoto, T.; Fujimori, H. (Fe–Co)–(Mg-fluoride) insulating nanogranular system with enhanced tunnel-type giant magnetoresistance. *J. Appl. Phys.* **2001**, *90*, 4159–4162. [[CrossRef](#)]
- von Helmolt, R.; Wecker, J.; Holzapfel, B.; Schultz, L.; Samwer, K. Giant negative magnetoresistance in perovskitelike  $\text{La}_{2/3}\text{Ba}_{1/3}\text{MnO}_x$  ferromagnetic films. *Phys. Rev. Lett.* **1993**, *71*, 2331–2334. [[CrossRef](#)] [[PubMed](#)]
- Hwang, H.Y.; Cheong, S.-W.; Ong, N.P.; Batlogg, B. Spin-polarized intergrain tunnelling in  $\text{La}_{2/3}\text{Sr}_{1/3}\text{MnO}_3$ . *Phys. Rev. Lett.* **1996**, *75*, 2041–2044. [[CrossRef](#)] [[PubMed](#)]
- Kim, T.H.; Uehara, M.; Cheong, S.-W.; Lee, S. Large room-temperature intergrain magnetoresistance in double perovskite  $\text{SrFe}_{1-x}(\text{Mo or Re})_x\text{O}_3$ . *Appl. Phys. Lett.* **1999**, *74*, 1737–1739. [[CrossRef](#)]
- Niebieskikwiat, D.; Caneiro, A.; Sánchez, R.D.; Fontcuberta, J. Oxygen-induced grain boundary effects on magnetotransport properties of  $\text{Sr}_2\text{FeMoO}_6$ . *Phys. Rev. B Cover. Condens. Matter Mater. Phys.* **2001**, *64*, 180406. [[CrossRef](#)]
- Sharma, A.; Berenov, A.; Rager, J.; Branford, W.; Bugoslavsky, Y.; Cohen, L.F.; MacManus-Driscoll, J.L. Enhanced intergrain magnetoresistance in bulk  $\text{Sr}_2\text{FeMoO}_6$  through controlled processing. *Appl. Phys. Lett.* **2003**, *83*, 2384–2386. [[CrossRef](#)]
- Gaur, A.; Varma, G.D. Enhanced magnetoresistance in double perovskite  $\text{Sr}_2\text{FeMoO}_6$  through  $\text{SrMoO}_4$  tunneling barriers. *Mater. Sci. Eng. B* **2007**, *143*, 64–69. [[CrossRef](#)]
- Suchanek, G.; Kalanda, N.; Artiukh, E.; Yarmolich, M.; Sobolev, N.A. Tunneling conduction mechanisms in strontium ferromolybdate ceramics with strontium molybdate dielectric intergrain barriers. *J. Alloys Compd.* **2020**, *860*, 158526. [[CrossRef](#)]
- Serrate, D.; De Teresa, J.M.; Ibarra, M.R. Double perovskites with ferromagnetism above room temperature. *J. Phys. Condens. Matter.* **2006**, *19*, 023201. [[CrossRef](#)]
- Yuan, C.L.; Zhu, Y.; Ong, P.P.; Ong, C.K.; Yu, T.; Shen, Z.X. Grain boundary effects on the magneto-transport properties of  $\text{Sr}_2\text{FeMoO}_6$  induced by variation of the ambient  $\text{H}_2$ -Ar mixture ratio during annealing. *Physica* **2003**, *334*, 408–412. [[CrossRef](#)]
- Suchanek, G. Tunnel magnetoresistance of granular superparamagnetic and ferrimagnetic structures. *Nanomater. Sci. Eng.* **2022**, *4*, 10–20. [[CrossRef](#)]
- Flynn, H.G. Physics of Acoustic Cavitations in Liquids. In *Physical Acoustics*, 1st ed.; Mason, W.P., Ed.; Academic Press: New York, NY, USA, 1964; Volume 1, Part B, pp. 57–172.
- Gedanken, A. Using sonochemistry for the fabrication of nanomaterials. *Ultrason. Sonochem.* **2004**, *11*, 47–55. [[CrossRef](#)] [[PubMed](#)]
- Demyanov, S.; Kalanda, N.; Yarmolich, M.; Petrov, A.; Lee, S.H.; Yu, S.C.; Oh, S.K.; Kim, D.H. Characteristic features of the magnetoresistance in the ferrimagnetic ( $\text{Sr}_2\text{FeMoO}_{6-\delta}$ )—dielectric ( $\text{SrMoO}_4$ ) nanocomposite. *AIP Adv.* **2018**, *8*, 055919. [[CrossRef](#)]
- Kalanda, N.; Yarmolich, M.; Teichert, S.; Bohmann, A.; Petrov, A.; Moog, D.; Mathur, S. Charge transfer mechanisms in strontium ferromolybdate with tunneling barriers. *J. Mater. Sci.* **2018**, *53*, 8347–8354. [[CrossRef](#)]
- Sheng, P.; Abeles, B.; Arie, Y. Hopping conductivity in granular metals. *Phys. Rev. Lett.* **1973**, *31*, 44–47. [[CrossRef](#)]
- Abeles, B.; Sheng, P.; Coutts, M.D.; Arie, Y. Structural and electrical properties of granular metal films. *Adv. Phys.* **1975**, *24*, 407–461. [[CrossRef](#)]
- Helman, J.S.; Abeles, B. Tunneling of spin-polarized electrons and magnetoresistance in granular Ni films. *Phys. Rev. Lett.* **1976**, *37*, 1429–1432. [[CrossRef](#)]
- Mitani, S.; Takahashi, S.; Takanashi, K.; Yakushiji, K.; Maekawa, S.; Fujimori, H. Enhanced magnetoresistance in insulating granular systems: Evidence for higher-order tunneling. *Phys. Rev. Lett.* **1998**, *81*, 2799–2802. [[CrossRef](#)]
- Fisher, B.; Genossar, J.; Chashka, K.B.; Patlagan, L.; Reisner, G.M. Intergrain tunnelling in the half-metallic double-perovskites  $\text{Sr}_2\text{BB}'\text{O}_6$  ( $\text{BB}' = \text{FeMo, FeRe, CrMo, CrW, CrRe}$ ). *EPJ Web Conf.* **2014**, *75*, 01001. [[CrossRef](#)]
- Xu, Y.; Ephron, D.; Beasley, M.R. Directed inelastic hopping of electrons through metal-insulator-metal tunnel junctions. *Phys. Rev. B Condens. Matter Mater. Phys.* **1995**, *52*, 2843–2859. [[CrossRef](#)]
- Inoue, J.; Maekawa, S. Theory of tunneling magnetoresistance in granular magnetic films. *Phys. Rev. B Condens. Matter Mater. Phys.* **1996**, *53*, R11927–R11929. [[CrossRef](#)]
- Serrate, D.; De Teresa, J.M.; Algarabel, P.A.; Ibarra, M.R.; Galibert, J. Intergrain magnetoresistance up to 50 T in the half-metallic  $(\text{Ba}_{0.8}\text{Sr}_{0.2})_2\text{FeMoO}_6$  double perovskite: Spin-glass behavior of the grain boundary. *Phys. Rev. B Condens. Matter Mater. Phys.* **2005**, *71*, 104409. [[CrossRef](#)]
- Bean, C.P.; Livingston, J.D. Superparamagnetism. *J. Appl. Phys.* **1959**, *30*, 1205–1295. [[CrossRef](#)]

26. Pierce, D.T.; Celotta, R.J.; Unguris, J.; Siegmann, H.C. Spin-dependent elastic scattering of electrons from a ferromagnetic glass, Ni<sub>40</sub>Fe<sub>40</sub>B<sub>20</sub>. *Phys. Rev. B Condens. Matter Mater. Phys.* **1982**, *26*, 2566–2574. [[CrossRef](#)]
27. MacDonald, A.H.; Jungwirth, T.; Kasner, M. Temperature dependence of itinerant electron junction magnetoresistance. *Phys. Rev. Lett.* **1998**, *81*, 705–708. [[CrossRef](#)]
28. Bloch, F. Zur Theorie des Ferromagnetismus. *Z. Phys.* **1930**, *61*, 206–219. [[CrossRef](#)]
29. Mauri, D.; Scholl, D.; Siegmann, H.C.; Kay, E. Observation of the exchange interaction at the surface of a ferromagnet. *Phys. Rev. Lett.* **1988**, *61*, 758–761. [[CrossRef](#)] [[PubMed](#)]
30. Shang, C.H.; Nowak, J.; Jansen, R.; Mooder, J.S. Temperature dependence of magnetoresistance and surface magnetization in ferromagnetic tunnel junctions. *Phys. Rev. B Condens. Matter Mater. Phys.* **1998**, *58*, R2917–R2920. [[CrossRef](#)]
31. Garcia, V.; Bibes, M.; Barthélémy, A.; Bowen, M.; Jacquet, E.; Contour, J.-P.; Fert, A. Temperature dependence of the interfacial spin polarization of La<sub>2/3</sub>Sr<sub>1/3</sub>MnO<sub>3</sub>. *Phys. Rev. B Condens. Matter Mater. Phys.* **2004**, *69*, 052403. [[CrossRef](#)]
32. Balcells, L.I.; Navarro, J.; Bibes, M.; Roig, A.; Martínez, B.; Fontcuberta, J. Cationic ordering control of magnetization in Sr<sub>2</sub>FeMoO<sub>6</sub> double perovskite. *Appl. Phys. Lett.* **2001**, *78*, 781–783. [[CrossRef](#)]
33. Suchaneck, G. Tunnel Spin-Polarization of ferromagnetic metals and ferrimagnetic oxides and its effect on tunnel magnetoresistance. *Electron. Mater.* **2022**, *3*, 227–234. [[CrossRef](#)]
34. Vidya, S.; John, A.; Solomon, S.; Thomas, J.K. Optical and dielectric properties of SrMoO<sub>4</sub> powders prepared by the combustion synthesis method. *Adv. Mater. Res.* **2012**, *1*, 191–204. [[CrossRef](#)]
35. Wang, K.; Sui, Y. Influence of the modulating interfacial state on Sr<sub>2</sub>FeMoO<sub>6</sub> powder magnetoresistance properties. *Solid State Commun.* **2004**, *129*, 135–138. [[CrossRef](#)]
36. Alvarado-Flores, J.J.; Mondragón-Sánchez, R.; Ávalos-Rodríguez, M.L.; Alcaraz-Vera, J.V.; Rutiaga-Quiñones, J.G.; Guevara-Martínez, S.J. Synthesis, characterization and kinetic study of the Sr<sub>2</sub>FeMoO<sub>6-δ</sub> double perovskite: New findings on the calcination of one of its precursors. *Int. J. Hydrog. Energy* **2021**, *46*, 26185–26196. [[CrossRef](#)]
37. Artiukh, E.; Suchaneck, G. Intergranular magnetoresistance of strontium ferromolybdate ceramics caused by spin-polarized tunneling. *Open Ceram.* **2021**, *7*, 100171. [[CrossRef](#)]
38. Kobayashi, K.I.; Kimura, T.; Sawada, H.; Terakura, K.; Tokura, Y. Room-temperature magnetoresistance in an oxide material with an ordered double-perovskite structure. *Nature* **1998**, *395*, 677–680. [[CrossRef](#)]
39. Brown, W.F. Theory of the approach to magnetic saturation. *Phys. Rev.* **1940**, *58*, 736–743. [[CrossRef](#)]
40. Brown, W.F. *Micromagnetics*, 1st ed.; Interscience Publisher: New York, NY, USA, 1963.
41. Zhang, H.; Zeng, D.; Liu, Z. The law of approach to saturation in ferromagnets originating from the magnetocrystalline anisotropy. *J. Magn. Magn. Mater.* **2010**, *322*, 2375–2380. [[CrossRef](#)]
42. Yoon, D.H.; Muksin; Raju, K. Controlling the magnetic properties of nickel ferrites by doping with different divalent transition metal (Co, Cu, and Zn) cations. *J. Supercond. Nov. Magn.* **2016**, *29*, 439–445. [[CrossRef](#)]
43. Cullity, B.D.; Graham, C.D. *Introduction to Magnetic Materials*, 2nd ed.; Wiley: Hoboken, NJ, USA, 2009.
44. Navarro, J.; Nogués, J.; Muñoz, J.S.; Fontcuberta, J. Antisites and electron-doping effects on the magnetic transition of Sr<sub>2</sub>FeMoO<sub>6</sub>. *Phys. Rev. B Condens. Matter Mater. Phys.* **2003**, *67*, 174416. [[CrossRef](#)]
45. Navarro, J.; Balcells, L.I.; Sandiumenge, F.; Bibes, M.; Roig, A.; Martínez, B.; Fontcuberta, J. Antisite defects and magnetoresistance in Sr<sub>2</sub>FeMoO<sub>6</sub> double perovskite. *J. Phys. Condens. Matter* **2001**, *13*, 8481–8488. [[CrossRef](#)]
46. Matin, M.A.; Hossain, M.N.; Hakim, M.A.; Islam, M.F. Effects of Gd and Cr co-doping on structural and magnetic properties of BiFeO<sub>3</sub> nanoparticles. *Mater. Res. Express* **2019**, *6*, 055038. [[CrossRef](#)]
47. Brown, W.F. The effect of dislocations on magnetization near saturation. *Phys. Rev.* **1941**, *60*, 139–147. [[CrossRef](#)]
48. Néel, L. La loi d’approche en a: H et une nouvelle théorie de la dureté magnétique. *J. Phys. Radium* **1948**, *9*, 184–192. [[CrossRef](#)]
49. Grady, D.E. Origin of the linear term in the expression for the approach to saturation in ferromagnetic materials. *Phys. Rev. B Condens. Matter Mater. Phys.* **1971**, *4*, 3982–3989. [[CrossRef](#)]
50. Suchaneck, G.; Kalanda, N.; Yarmolich, M.; Artiukh, E.; Gerlach, G.; Sobolev, N.A. Magnetization of magnetically inhomogeneous Sr<sub>2</sub>FeMoO<sub>6-δ</sub> nanoparticles. *Electron. Mater.* **2022**, *3*, 82–92. [[CrossRef](#)]
51. Kalanda, N.; Yarmolich, M.; Burko, A.; Temirov, A.; Kislyuk, A.; Demyanov, S.; Lenz, K.; Lindner, J.; Kim, D.-H. Superparamagnetism and ferrimagnetism in the Sr<sub>2</sub>FeMoO<sub>6-δ</sub> nanoscale powder. *Ceram. Int.* **2022**, *48*, 23931–23937. [[CrossRef](#)]
52. Akulov, N.S. Über den Verlauf der Magnetisierungskurve in starken Feldern. *Z. Phys.* **1931**, *69*, 822–831. [[CrossRef](#)]
53. Nosach, T.; Mullady, G.; Leifer, N.; Adyam, V.; Li, Q.; Greenbaum, S.; Ren, Y. Angular dependence of spin-wave resonance and relaxation in half-metallic Sr<sub>2</sub>FeMoO<sub>6</sub> films. *J. Appl. Phys.* **2008**, *103*, 07E311. [[CrossRef](#)]
54. Suchaneck, G.; Artiukh, E. Magnetoresistance of Antiphase Boundaries in Sr<sub>2</sub>FeMoO<sub>6-δ</sub>. *Phys. Status Solidi B* **2022**, *259*, 2100353. [[CrossRef](#)]
55. Becker, R.; Polley, H. Der Einfluß innerer Spannungen auf das Einmüdungsgesetz bei Nickel. *Ann. Phys.* **1940**, *429*, 534–540. [[CrossRef](#)]
56. Bozorth, R.M.; Tilden, E.F.; Williams, A.J. Anisotropy and magnetostriction of some ferrites. *Phys. Rev.* **1955**, *99*, 1788–1798. [[CrossRef](#)]
57. Alam, M.; Kalyan, M.; Khan, G.G. Origin and tuning of room temperature ferromagnetism and ferroelectricity in double perovskite Y<sub>2</sub>NiMnO<sub>6</sub> nanostructured thin films. *J. Alloys Compd.* **2020**, *822*, 153540. [[CrossRef](#)]

58. Vergne, R. L'approche à la saturation de l'aimantation des corps ferromagnétiques polycristallins de structure cubique. *Phys. Status Solidi* **1966**, *14*, 143–147. [[CrossRef](#)]
59. Grössinger, R.A. Critical Examination of the Law of Approach to Saturation, I. Fit Procedure. *Phys. Status Solidi A* **1981**, *66*, 665–674. [[CrossRef](#)]
60. Evans, R.F.L.; Atxitia, U.; Chantrell, R.W. Quantitative simulation of temperature-dependent magnetization dynamics and equilibrium properties of elemental ferromagnets. *Phys. Rev. B Condens. Matter Mater. Phys.* **2015**, *91*, 144425. [[CrossRef](#)]
61. Tedrow, P.M.; Meservey, R. Spin polarization of electrons tunneling from films of Fe, Co, Ni, and Gd. *Phys. Rev. B Condens. Matter Mater. Phys.* **1973**, *7*, 318–326. [[CrossRef](#)]
62. Ferromagnetic Curie Temperatures. Available online: <http://hyperphysics.phy-astr.gsu.edu/hbase/Tables/Curie.html> (accessed on 12 November 2023).
63. Paul, A.A. Estimation of Magnetic Anisotropy in Ferromagnetic Elements and Their Alloy Powders by the Law of Approach to Saturation (LAS). Master's Thesis, Department of Mechanical Engineering in the University of Michigan-Dearborn, Dearborn, MI, USA, 2020; p. 26. [[CrossRef](#)]
64. Wang, J.-F.; Li, Z.; Xu, X.-J.; Gu, Z.-B.; Yuan, G.-L.; Zhang, S.-T. The competitive and combining effects of grain boundary and Fe/Mo antisite defects on the low-field magnetoresistance in Sr<sub>2</sub>FeMoO<sub>6</sub>. *J. Am. Ceram. Soc.* **2014**, *97*, 1137–1142. [[CrossRef](#)]
65. Kalanda, N.; Karpinsky, D.; Bobrikov, I.; Yarmolich, M.; Kuts, V.; Huang, L.; Hwang, C.; Kim, D.-H. Interrelation among superstructural ordering, oxygen nonstoichiometry and lattice strain of double perovskite Sr<sub>2</sub>FeMoO<sub>6-δ</sub> materials. *J. Mater. Sci.* **2021**, *56*, 11698–11710. [[CrossRef](#)]

**Disclaimer/Publisher's Note:** The statements, opinions and data contained in all publications are solely those of the individual author(s) and contributor(s) and not of MDPI and/or the editor(s). MDPI and/or the editor(s) disclaim responsibility for any injury to people or property resulting from any ideas, methods, instructions or products referred to in the content.